

THE UNIVERSITY of EDINBURGH

Edinburgh Research Explorer

Geometric control of 3D needle steering in soft-tissue

Citation for published version:
Khadem, M, Rossa, C, Usmani, N, Sloboda, RS & Tavakoli, M 2019, 'Geometric control of 3D needle steering in soft-tissue', *Automatica*, vol. 101, pp. 36-43. https://doi.org/10.1016/j.automatica.2018.11.018

Digital Object Identifier (DOI):
10.1016/j.automatica.2018.11.018

Link:
Link to publication record in Edinburgh Research Explorer

Document Version:
Peer reviewed version

Published In:
Automatica

General rights
Copyright for the publications made accessible via the Edinburgh Research Explorer is retained by the author(s) and / or other copyright owners and it is a condition of accessing these publications that users recognise and abide by the legal requirements associated with these rights.

Take down policy
The University of Edinburgh has made every reasonable effort to ensure that Edinburgh Research Explorer content complies with UK legislation. If you believe that the public display of this file breaches copyright please contact openaccess@ed.ac.uk providing details, and we will remove access to the work immediately and investigate your claim.



Download date: 29. Mar. 2024

This paper appears in journal of Automatica
Content may change prior to publication
DOI: https://doi.org/10.1016/j.automatica.2018.11.018

Geometric Control of 3D Needle Steering in Soft-Tissue

Mohsen Khadem [a], Carlos Rossa [b], Nawaid Usmani [c], Ron S. Sloboda [c], Mahdi Tavakoli [d],

[a] *School of Informatics, University of Edinburgh, Edinburgh, UK.*

[b] *Department of Automotive, Mechanical and Manufacturing Engineering, University of Ontario, Canada.*

[c] *Cross Cancer Institute and the Department of Oncology, University of Alberta, Edmonton, Canada.*

[d] *Department of Electrical and Computer Engineering, University of Alberta, Edmonton, Canada.*

Abstract

In this paper, a 3D automated needle steering system is presented that can enhance the performance of needle-based procedures. The system comprises a nonholonomic needle steering model and a nonlinear controller for 3D needle steering. First, a reduced-order needle steering model is presented. Next, a geometric reduction procedure is carried out to present the nonlinear control system in a transformed format. Finally, the transformed model is used to design a two-step controller. The controller first stabilizes the system on an equilibrium manifold of the system and later employs a switching law to stabilize it on an equilibrium point in the manifold. The former performs insertion of the needle up to a desired depth and the latter performs retraction/insertion motion that guides the needle toward a desired point at the given depth. Validation experiments are performed on a phantom and ex-vivo animal tissues and the results are compared with manual needle insertions performed by skilled surgeons. The mean error of our 3D needle steering system is 60% less than manual needle insertions.

Key words: Geometric approaches, Medical applications, Autonomous control, Robot control

1 Introduction

In needle-based interventions, flexible needles with beveled tips are steered in soft tissue to reach designated targets. A needle with an asymmetric beveled tip has an uneven distribution of forces at the tip, which causes the needle to deflect from a straight path during the insertion. During the procedure, the surgeon controls the needle tip deflection by axially rotating the needle's base, thus changing the orientation of the beveled tip. Here, we present a new approach for automatic needle steering from any point to any other point that can be used to reach targets in 3D. Inspired by clinical needle insertions, we propose a systematic two-step needle steering approach. The first step involves insertion of the needle with proper axial rotations to reach to the proximity of a desired target in 3D. Due to uncertainties in needle-tissue interaction the needle might not reach the target. To compensate for these effects, a series of retractions and insertions are performed in the second step to precisely steer the needle toward the desired location.

Modeling and control of robotic needle steering has been widely studied [1, 8, 14, 19]. Park *et al.* developed a nonholonomic unicycle-like model to describe needle deflection in firm tissue [14]. They assumed that the needle tip motion in tissue is constrained to a circular path similar to a unicycle mobile robot. Webster *et al.* extended this idea and developed a kinematics-based model generalizing the unicycle model [19]. Several research groups have used classical beam theories to develop models of needle deflection [8, 17]. The nonholonomic unicycle model [19] is commonly used for needle steering. Kallem and Cowan presented the unicycle model in generalized coordinates and used feedback linearization approach for 2D needle steering [6]. Minhas *et al.* presented the idea of duty-cycled spinning of the needle during insertion and showed that the curvature of the needle can be con-

⋆ This paper was not presented at any IFAC meeting. Corresponding author M.Khadem.

Email addresses: mohsen.khadem@inf.ed.ac.uk (Mohsen Khadem), Carlos.Rossa@uoit.ca (Carlos Rossa), nawaid.usmani@albertahealthservices.ca (Nawaid Usmani), ron.sloboda@albertahealthservices.ca (Ron S. Sloboda), mahdi.tavakoli@ualberta.ca (Mahdi Tavakoli).

trolled via periodic needle rotations [12]. Rucker *et al.* proposed a sliding-mode controller based on the unicycle model and used it to track a desired trajectory within the tissue [16]. Patil *et al.* developed a needle steering strategy that relies on a rapid motion planner [15]. The planner incorporates the unicycle model to calculate the optimal needle axial rotations for steering the needle in 3D. From our group, Khadem *et al.* implemented the unicycle model in an online motion planner to perform 2D surgeon-in-the-loop needle steering [10].

The needle steering system is a nonlinear constrained system and most of the system states, namely, needle tip position and orientation, cannot be directly measured from 2D imaging systems. Thus, most of the presented needle steering strategies can only steer the needle in 2D [6, 7, 12]. Several 3D needle steering algorithms are developed by incorporating image-based algorithms for calculating the needle pose in 2D ultrasound images and consequently estimating unicycle model parameters [15]. However, no proof of convergence or stability were provided. Also, to the best of the authors' knowledge, none of the previous studies propose a method for correcting final targeting error that can occur due to many factors such as uncertain tissue interactions or target motion.

Here, we propose a nonholonomic model of needle steering. Next, we use the model to design a two-step controller that inserts the needle up to the desired depth and as close as possible to the desired target location, and later performs a series of retraction and insertion motions that guides the needle toward the desired point. To the best of the author's knowledge, this is the first 3D needle steering system that incorporates the retraction/insertion of the needle – which is common in clinical needle insertions – to precisely steer the needle to a desired point. This paper is organized as follows: Section II describes the 3D kinematic model of needle steering and details the geometric reduction method employed to transform the system into a simpler form. Design of the controller is presented in Section III. The simulation and experimental results are discussed and compared with manual insertions in Section IV.

2 Nonholonomic Model of Needle Steering

Here, we briefly introduce a nonholonomic model of needle steering first presented in [9]. Next, we use a geometric tool known as *connections* and transform the system's model to a reduced form known as the *normal form* [2].

2.1 Kinematic Model of Needle Steering

The model is inspired by the work in [19] and assumes that the needle tip bends under the asymmetric distribution of forces applied to the beveled tip and follows a path with a constant radius of curvature in a plane defined by the orientation of the needle beveled tip. Fig. 1 shows a schematic of 3D needle steering in tissue. The configuration space of the needle tip can be parametrized by the general coordinates $q = [x, y, z, \phi, \theta]^T$, denoting the position of the needle tip in 3D, the orientation of the needle tip (roll angle), and the angle of the needle tip as it deflects (pitch angle). Let $v, \omega \in \mathbb{R}$ denote the needle insertion and rotation velocities expressed in the local frame. Following the approach proposed in [9], we can build the nonholonomic model of needle steering as

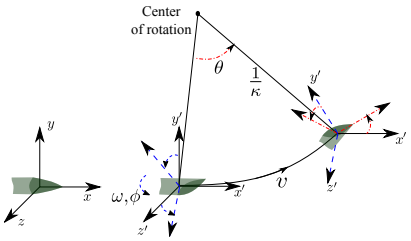


Figure 1. A schematic of needle steering in tissue. An inertial coordinate frame xyz is fixed at the needle point of entry and a local body-fixed frame $x'y'z'$ attached to the needle tip initially coincides with the inertial frame. The needle follows a curved path in $x'y'$ plane while rotating around the z'-axis with an angle of θ. The needle can also rotate axially about x' by an angle ϕ. The needle tip motion can be fully defined by a set of generalized coordinates $q = [x, y, z, \phi, \theta]^T$.

$$\dot{q} = [\mathrm{C}\theta \;\; \mathrm{S}\theta\mathrm{C}\phi \;\; \mathrm{S}\theta\mathrm{S}\phi \;\; 0 \;\; \kappa]^T v + [0\ 0\ 0\ 1\ 0]^T \omega. \quad (1)$$

Throughout this paper, shorthand notations S and C describe $\sin(\cdot)$ and $\cos(\cdot)$, respectively.

Remark. Let q^e denote an equilibrium solution of the system in (1) corresponding to $v = \omega = 0$. The following observations can be made:
1) The system in (1) is driftless and affine in the inputs. Using successive Lie brackets, it can be shown that the rank of the system's accessibility distribution is 5. Thus, the system is controllable at q^e.
2) Based on the Brockett's theory (see [4]), a necessary condition for the existence of c^1 asymptotically stabilizing feedback law for (1) is that the image of the mapping $(q, v, w) \rightarrow (v\mathrm{C}\theta, v\mathrm{S}\theta\mathrm{C}\phi, v\mathrm{S}\theta\mathrm{S}\phi, \omega, \kappa v)$ contain some neighbourhood of q^e. The system fails to satisfy this condition. For instance, in a neighbourhood of zero, where $\kappa v = 0$, i.e., $v = 0$, no points of the form $[\epsilon\ 0\ 0\ 0\ 0]^T$, $\epsilon \neq 0$ are in its image. Thus, the system is not asymptotically staibilizable using a smooth feedback law.

Based on the above discussion, a single equilibrium of (1) cannot be asymptotically stabilized using a control approach that uses smooth feedback. Here we propose a non-smooth two-step control strategy that stabilizes the system to an equilibrium sub-manifold of the system via smooth feedback and later uses a switching law to stabilize the system on an equilibrium point. But first, we use the theory of *connections* to transform the system's

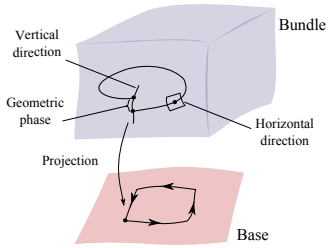


Figure 2. A graphical representation of the bundle and connections. A connection divides the space into vertical and horizontal directions.

model to a *normal form* that is easy to analyze. The presented transformation has been studied in [11] and is formed by viewing the configuration manifold as the total space of a fiber bundle.

2.2 Geometric Model Reduction

Fiber bundle is a mapping that projects a larger space called bundle $\mathcal{Q}$ onto a smaller one called the base B, as in Fig. 2. In a trivial case (such as ours), the space $\mathcal{Q}$ is $B \times F$, where F is called the fiber. The similarity between $\mathcal{Q}$ and a product space $B \times F$ is defined using a continuous surjective projection $\Pi : \mathcal{Q} \to B$. We show that the nonholonomic model of needle steering in (1) can be described as a fiber bundle. Considering the configuration space of the system $\mathcal{Q}$ parametrized by q is the total space of the fiber bundle and the base space B is parametrized by the local coordinates b, we can divide the general coordinates to $q = (b, p) \in \mathbb{R}^2 \times \mathbb{R}^3$, where $b = [\phi \ \ \theta]^T$ is the base space coordinate and $p = [x \ \ y \ \ z]^T$ is the fiber coordinate. Using (1) we can write the mapping from the base coordinates b to the general coordinates q as

$$\dot{q} = C^T \dot{b} \ , \tag{2}$$

where $C = [-J \ \ I]$, I is a 2×2 identity matrix, and

$$J = \begin{bmatrix} 0 & 0 & 0 \\ -\frac{\mathrm{C}\theta}{\kappa} & -\frac{\mathrm{S}\theta\mathrm{C}\phi}{\kappa} & -\frac{\mathrm{S}\theta\mathrm{S}\phi}{\kappa} \end{bmatrix}. \tag{3}$$

Based on (2), the system's configuration space solely depends on the evolution of the base coordinates and the base space describes the internal shape of the system. This is one of the features of a fiber bundle mapping. In lieu of (1), we rewrite the nonholonomic model in a normal form given below using (2)

$$\begin{aligned} \dot{b} =& u, \\ \dot{p} =& -J^T u, \\ \dot{u} =& U, \end{aligned} \tag{4}$$

where $U = [\kappa\dot{v} \ \ \dot{\omega}]$. Based on (4), the base space is the control space, in the sense that the path in the base space can be chosen by suitable control inputs.

We now analyse the motion of the system along the fibers in more details. As shown above, the motion generation in a fiber bundle can be viewed as a question of relating internal changes in a base space to net changes in the bundle. Directions of motion in the bundle space $\mathcal{Q}$ that project to zero on base space B are called vertical directions. Horizontal directions are the set of directions that complement the space of vertical directions. For a horizontal motion in the bundle corresponding to a cyclic motion in the base, the vertical motion will undergo a shift in the vertical space V, called the *geometric phase* (see Fig. 2). We can define the connection $\mathbf{w} : T\mathcal{Q} \to V$ as a vector valued projection from the tangent bundle of $\mathcal{Q}$ onto its vertical part, given by

$$\mathbf{w} = (dp + J^T db)\frac{\partial}{\partial p}. \tag{5}$$

In terms of coordinates, $\mathbf{w}$ maps $(\dot{b}, \dot{p})$ onto $(0, \dot{p} + J^T\dot{b})$. Now, suppose we have a loop in the base with p starting at p_0, the geometric phase can be obtained using (5) as

$$p_f - p_o = -\oint J^T db, \tag{6}$$

where p_f is the final position in the fiber. Based on (6), the geometric phase depends on the area enclosed by the path in the base space and J. Let $\gamma(\phi^*, \theta^*)$ denote a closed path in base space, using (3) and (6) we have

$$\begin{aligned} x_f =& x_0 + \oint_\gamma \frac{\mathrm{C}\theta}{\kappa} d\theta, \quad y_f = y_0 + \oint_\gamma \frac{\mathrm{C}\phi\mathrm{S}\theta}{\kappa} d\theta, \\ z_f =& z_0 + \oint_\gamma \frac{\mathrm{S}\phi\mathrm{S}\theta}{\kappa} d\theta. \end{aligned} \tag{7}$$

If the closed loop in base is a path on a square starting at (ϕ_0, θ_0) and sequentially moving to (ϕ^*, θ_0), (ϕ^*, θ^*), $(0, \theta^*)$, $(0, \theta_0)$, and finally back to (ϕ_0, θ_0), using (7) we can obtain the geometric phase

$$\begin{aligned} x_f =& 0 \\ y_f =& y_0 - \frac{1}{\kappa}\mathrm{C}\phi^*(\mathrm{C}(\theta^*) - \mathrm{C}\theta_0) + \frac{1}{\kappa}(\mathrm{C}(\theta^*) - \mathrm{C}\theta_0) \\ z_f =& z_0 - \frac{1}{\kappa}\mathrm{S}\phi^*(\mathrm{C}(\theta^*) - \mathrm{C}\theta_0) \end{aligned} \tag{8}$$

Based on (8), the closed path in the base space will not move the needle in x direction but shifts the needle in y and z directions. As we will show later, the selected closed path simulates a retraction/insertion motion and is expected to keep the insertion depth (i.e., x) fixed. In the remainder of this paper, the geometric phase given by (7) and the normal form of the system in (4) will be used to design a needle steering controller

3 Controller Design

Let $q_0 = [x_0, y_0, z_0, \phi_0, \theta_0]^T$ denote an initial state. The design of a control strategy that transfers the initial state to an equilibrium point $q_e = [x_e, y_e, z_e, \phi_e, \theta_e]^T$ involves the following two-steps: (1) Stabilize the system on an equilibrium manifold. The equilibrium manifold is selected based on certain clinical metrics with the intention of steering the needle to the desired depth, x_e, while bringing the needle as close as possible to the desired equilibrium point (x_e, y_e, z_e). The coordinate of the system on the equilibrium manifold is $q_1 = [x_e, y_1, z_1, \phi_e, \theta_e]^T$. (2) Traverse a closed path in the base space to produce a retraction/insertion motion that brings q_1 to q_e.

3.1 Step 1: Stabilization on a Manifold

In this section, we study the problem of smooth stabilization of the needle to an equilibrium sub-manifold of $\mathcal{Q}$. The equilibrium sub-manifold is given by

$$\mathcal{Q}_e = \{(q, \dot{q}) \mid \dot{q} = 0, f(q) = 0\}\ , \tag{9}$$

where $f(q)$ is a smooth vector function. We extend the results of [3] to design a feedback control law such that the closed loop has a locally asymptotically stable point on $\mathcal{Q}_e$. We consider the following control law

$$U = -\left(\frac{\partial f}{\partial q}C^T\right)^{-1}\left[\frac{\partial}{\partial q}\left(\frac{\partial f}{\partial q}C^T\dot{b}\right)C^T\dot{b} + K_1\frac{\partial f}{\partial q}C^T\dot{b} + K_2 f\right] \tag{10}$$

with K_1 and K_2 denoting constant symmetric positive definite 2×2 matrices. The proposed control law renders $(q, \dot{q}) \rightarrow \mathcal{Q}_e$ if the transversality condition $\det\left(\frac{\partial f}{\partial b}\right)\det\left(\frac{\partial f}{\partial q}C^T\right) \neq 0$ is satisfied. For detailed proof of the convergence and stability refer to [3].

The transversality condition ensures that the model in normal form (4) and the mapping $(b, p, \dot{b}) \rightarrow (f, p, \dot{f})$ is a diffeomorphism. To satisfy it, $f(q)$ in (9) should be a smooth 2-dimensional vector function and include the base coordinates θ and ϕ. To define $f(q)$, we remark that in practice needles are inserted at relatively high velocities to eliminate the effect of uncertainties in targeting error, and later retraction/insertions can be made to compensate for targeting errors (if there is any). Denoting the desired final equilibrium point as $q_e = [x_e, y_e, z_e, \phi_e, \theta_e]^T$ and inspired by clinical needle insertion approach we define $f(q)$ as

$$f_1 = \theta + \phi + (y - y_e)^2 + (z - z_e)^2 - k_{0,1} \tag{11a}$$
$$f_2 = \theta + (x - x_e)^2 - k_{0,2} \tag{11b}$$

The first element of $f(q)$ is defined in order to minimize the targeting error in y and z directions by modulating θ and ϕ corresponding to insertion velocity and axial rotation velocity, respectively. $k_{0,1}$ is a constant parameter that can be tuned to increase needle insertion and axial rotation velocities while minimizing the targeting error. When the system is stabilized on the equilibrium manifold, i.e., $f_1 = f_2 = 0$, the final targeting error is equal to $k_{0,1} - \theta_e - \phi_e$. The second element aims to steer the needle to the desired insertion depth x_e. As $f_2 \rightarrow 0$, needle insertion depth error $\parallel x - x_e \parallel$ goes to $\pm\sqrt{k_{0,2} - \theta_e}$. From (7) we can obtain $\theta_e = \text{asin}(x_e\kappa)$ at the desired insertion depth x_e. Selecting $k_{0,2} = \theta_e$, guarantees the needle insertion depth error goes to zero. In the next section we design a non-smooth controller that stabilizes the system on an equilibrium point on the manifold.

3.2 Step 2: Stabilization to a Point

Considering the coordinate of the system on the equilibrium manifold is $q_1 = [x_e, y_1, z_1, \phi_e, \theta_e]^T$, we design a switching controller that brings the system from q_1 to $q_e = [x_e, y_e, z_e, \phi_e, \theta_e]^T$. The control design is based on the a priori selection of a closed path in the base space described in Section 2.2. We use the concept of geometric phase to select a path in base coordinate $\gamma(\phi^*, \theta^*)$ that brings the needle from q_1 to q_e. The main goal is to steer the needle in the base space (ϕ, θ) on a closed path to produce a desired geometric phase $(0, y_d, z_d)$, where $y_d = y_e - y_1$ and $z_d = z_e - z_1$.

We first consider a closed path in base space, γ_1, formed by the line segments from $b_e = (\phi_e, \theta_e)$ to $b_1 = (\phi^*, \theta_e)$, from b_1 to $b_2 = (\phi^*, \theta^*)$, from b_2 to $b_3 = (0, \theta^*)$, from b_3 to $b_4 = (0, \theta_e)$, and from b_4 back to $b_5 = b_e$ (Fig. 3 top left). Then, the geometric phase of the parametrized family is determined by (8). Solving (8) for (ϕ^*, θ^*), one can calculate the desired path in the base that will produce the desired geometric phase $(0, y_d, z_d)$. Solution of (8) and the corresponding selected closed path is given in the second row of Table. 1.

Note that when $y_d < 0$ or for $|\frac{y_d^2 + z_d^2}{y_d}| > \frac{4}{\kappa}\text{S}^2\frac{\theta_e}{2}$, θ^* is not analytic and the above described path is not applicable. Different paths can be selected for other initial conditions. The proposed paths and the corresponding base coordinates calculated by solving (7) in the closed form are shown in Fig. 3 and in Table. 1, respectively. Note that these paths are not unique and the desired phase geometry can be achieved via different paths or even concatenation of a series of closed paths.

Now, considering the bundle projection map, $\Pi : (b, p) \rightarrow (b)$, we define a family of feedback functions U_i^* such that for any $\Pi q(t_0)$ the solution of

$$\dot{b} = u \tag{12a}$$
$$\dot{u} = U_i^*(\Pi q) \tag{12b}$$

Table 1
Base coordinates for retraction/insertion motion of the needle. Corresponding closd paths are shown in Fig. 3. Note: $k \in \mathbb{Z}$, $y_d = y_e - y_1$, $z_d = z_e - z_1$.

	Condition	Path	Base coordinates	Needle motion
1	$z_d \mathrm{S}\phi_e \le 0,\ y_d \mathrm{C}\phi_e \le 0$	γ_4	$\phi_1^* = \pi - \phi_e,\ \phi_2^* = \pi + \phi_e,$ $\theta_1^* = \mathrm{acos}(-\frac{\kappa y_d}{2\mathrm{C}\phi_e} + \mathrm{C}\theta_e),\ \theta_2^* = \mathrm{acos}(-\frac{\kappa z_d}{2\mathrm{S}\phi_e} + \mathrm{C}\theta_e)$	double retraction–insertion
2	$z_d \in \mathbb{R},\ y_d \in \mathbb{R}^+$ & $\frac{y_d^2 + z_d^2}{y_d} \le \frac{4}{\kappa}\mathrm{S}^2\frac{\theta_e}{2}$	γ_1	$\phi^* = 2k\pi - 2\mathrm{atan}(y_d/z_d),\ \theta^* = \mathrm{acos}(\frac{\kappa y_d^2 + \kappa z_d^2}{2y_d} + \mathrm{C}\theta_e)$	retraction–insertion
3	$z_d \in \mathbb{R},\ y_d \in \mathbb{R}^-$ & $\frac{y_d^2 + z_d^2}{y_d} \ge -\frac{4}{\kappa}\mathrm{S}^2\frac{\theta_e}{2}$	γ_2	$\phi^* = 2k\pi - 2\mathrm{atan}(y_d/z_d),\ \theta^* = \mathrm{acos}(-\frac{\kappa y_d^2 + \kappa z_d^2}{2y_d} + \mathrm{C}\theta_e)$	retraction–insertion
4	$z_d \in \mathbb{R},\ y_d \in \mathbb{R}^+$ & $\frac{y_d^2 + z_d^2}{y_d} > \frac{4}{\kappa}\mathrm{S}^2\frac{\theta_e}{2}$	γ_2	$\phi^* = 2k\pi - 2\mathrm{atan}(y_d/z_d),\ \theta^* = -\mathrm{acos}(-\frac{\kappa y_d^2 + \kappa z_d^2}{2y_d} + \mathrm{C}\theta_e)$	retraction–insertion
5	$z_d \in \mathbb{R},\ y_d \in \mathbb{R}^-$ & $\frac{y_d^2 + z_d^2}{y_d} < -\frac{4}{\kappa}\mathrm{S}^2\frac{\theta_e}{2}$	γ_1	$\phi^* = 2k\pi - 2\mathrm{atan}(y_d/z_d),\ \theta^* = -\mathrm{acos}(\frac{\kappa y_d^2 + \kappa z_d^2}{2y_d} + \mathrm{C}\theta_e)$	retraction–insertion
6	$z_d \in \mathbb{R},\ y_d \in \mathbb{R}^+$ & $\frac{y_d^2 + z_d^2}{y_d} > \frac{4}{\kappa}\mathrm{S}^2\frac{\theta_e}{2}$	γ_2	$\phi^* = 2k\pi - 2\mathrm{atan}(y_d/z_d),\ \theta^* = \mathrm{acos}(-\frac{\kappa y_d^2 + \kappa z_d^2}{2y_d} + \mathrm{C}\theta_e)$	insertion–retraction
7	$z_d \in \mathbb{R},\ y_d \in \mathbb{R}^-$ & $\frac{y_d^2 + z_d^2}{y_d} < -\frac{4}{\kappa}\mathrm{S}^2\frac{\theta_e}{2}$	γ_1	$\phi^* = 2k\pi - 2\mathrm{atan}(y_d/z_d),\ \theta^* = \mathrm{acos}(\frac{\kappa y_d^2 + \kappa z_d^2}{2y_d} + \mathrm{C}\theta_e)$	insertion–retraction
8	$z_d \in \mathbb{R},\ y_d = 0$	γ_3	$\phi^* = 2k\pi + \mathrm{sign}(z_d)\pi/2,\ \theta^* = -\mathrm{acos}(-\mathrm{sign}(z_d)\frac{\kappa z_d}{2} + \mathrm{C}\theta_e)$	retraction–insertion

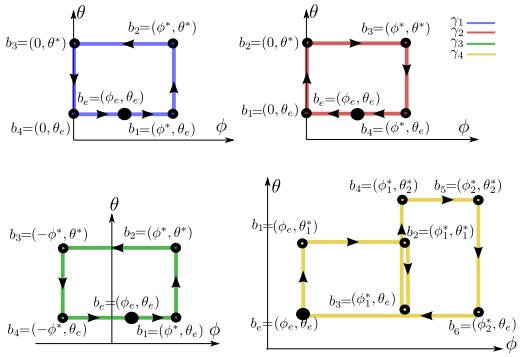


Figure 3. A graphical representation of closed paths in base coordinates corresponding to retraction/insertion of the needle. All the paths start from and end at (ϕ_e, θ_e).

satisfies $\Pi q(t_1) = (b_i, 0)$, where $t_1 > t_0$. The feedback function is parametrized by the vectors b_i, $i = 1, ..n$, where n is the number of line segments in the path. For each b_i, there exists such a feedback function. The control algorithm is constructed by appropriate switching between members of the family of feedback functions. On each cycle of the algorithm the particular functions selected depend on the closed path parameters. We propose the following PD feedback control law

$$\begin{cases} U_i^* = -k_{1,i}(b - b_i) - k_{2,i}\dot{b}, & \text{if } \Pi q \neq (b_i, 0) \\ U_i^* = 0, & \text{if } \Pi q = (b_i, 0) \end{cases} \quad (13)$$

where $k_{1,i}$ and $k_{2,i}$, $i = 1, ..n$, are arbitrary positive constants. It can be easily seen that the above feedback law asymptotically stabilizes (12). Now, we can construct the control algorithm as shown in Table 2. The inputs to the controller are the desired equilibrium point q_e, system's initial state on the equilibrium manifold q_1, and a tolerance ε which, if crossed, the goal equilibrium q_e is reached and the controller stops retraction/insertion.

Table 2
Needle steering algorithm

$U \leftarrow$ `Control_algorithm` (q_e, q_1, ε)

```
while ‖q_e − q_1‖ > ε do
    if z_d Sφ_e ≤ 0 & y_d Cφ_e ≤ 0
        γ = γ_1
    else
        Select γ from Table 1
    end
    Select (φ*, θ*) from Table 1 for desired geometric phase
    Construct the closed path b_i, i = 1, ..n
    for i = 1, ..., n do
        U = U_i*(Πq) until Πq = (b_i, 0)
    end
    q_1 ← q
end
```

Condition 1 in Table 1 corresponds to a steering scenario that includes a double retraction movement on previous insertion paths, one retraction to correct the error in y direction and another to correct insertion error in z direction. This is the primary control strategy as the needle is only retracted on the previous insertion paths. This is preferred as during the retraction the needle tends to follow the same path it has previously traversed during insertion. Results of the simulation for needle steering using condition 1 is shown in Fig. 4. In the simulation, the needle is steered to reach a target placed at a depth of 140 mm. The needle curvature in the simulations is $\kappa = 1/400\ \mathrm{mm}^{-1}$ [10]. The parameters of the first step controller are $K_1 = 100I$ and $K_2 = 10I$, where I is a 2×2 identity matrix, and $k_{0,1} = 0.3$ and $k_{0,1} = \mathrm{asin}(140\kappa)$. The parameters of the second controller are $k_{1,i} = k_{2,i} = 500$, $i = 1, .., 5$. As it can bee seen in Fig. 4, the controller retracts the needle on previous insertion paths using Condition 1. This condition can be employed when $z_d \mathrm{S}\phi_e \le 0$ and $y_d \mathrm{C}\phi_e \le 0$. To illustrate this condition, a schematic of 2D retraction when $\phi_e = 0$ is shown as well. In top right figure condition 1 is satisfied and retraction on prior insertion path is possible. However, when $(y - y_1)C\phi_e \ge 0$ (bottom right figure) it is clearly impossible to reach the target with a

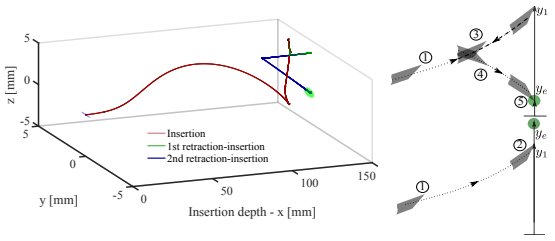
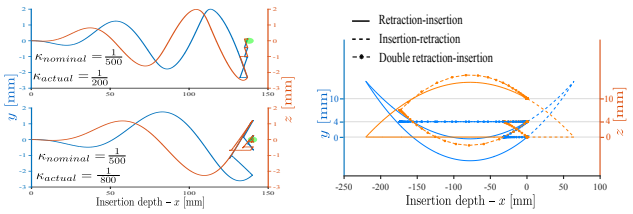


Figure 4. Simulation of double retractions on prior insertion paths using condition 1 in Table. 1. Schematics of 2D needle insertion and retraction for when condition 1 is satisfied and retraction on prior insertion path is possible (top right) and when it is is not satisfied (bottom right) are shown. Insertion and retractions are shown by dotted and dashed lines, respectively.



(a) (b)

Figure 5. (a)Results of the needle steering simulations with 60% uncertainty in the nominal value of radius of curvature. (b) A comparison between various options for needle retraction/insertion when the target point is far from the needle initial state.

retraction on the previously traversed insertion path.

Conditions 2 and 3 can be used when condition 1 is not satisfied. These conditions are designed for needle retraction-insertion motion assuming the needle follows the kinematics model prediction during retraction, i.e, retracted on path with curvature of κ. However, in practice the needle follows a different trajectory during retraction. To investigate this case, we simulate an extreme scenario in which the needle follows a retraction path with a curvature that is 60% smaller or bigger than the insertion curvature. Results are shown in Fig. 5(a). The controller is capable of steering the needle to the desired point by performing extra retractions. A total of 3 retractions are performed to reach the target with accuracy of 0.1 mm. Thus, even if the needle curvature during retraction is far from model predicted curvature, this strategy will still guide the needle to the desired target after several retraction-insertions.

In a very rare case that conditions 1, 2 and 3 are not satisfied, there are three possible options: 1) Use conditions 6 and 7 to further insert the needle to a higher depth and later retract the needle toward the target. 2) Use conditions 4 and 5 to perform an large retraction followed by a re-insertion (almost similar to a new insertion). 3) Perform multiple retractions and insertions using concatenation of a series of closed paths from conditions 1, 2, and 5. Several simulations are performed to illustrate these scenarios. It is assumed that the needle initial coordinate is (0,0,0) and the final target point is (0,4,10), the initial orientation ϕ_e and deflection angle θ_e are 0 and $\pi/10$, respectively. Three possible options are simulated and presented in Fig. 5(b). In the next section we perform several needle steering experiments in ex-vivo tissue to validate the proposed control strategy.

4 Experimental Evaluation

Here, needle insertion experiments are performed using the setup introduced in [18] to evaluate the designed needle steering controller. In the experiments, a ultrasound probe is robotically moved to follow the needle tip. The procedure introduced in [18] is used to calculate needle deflection along y and z directions from 2D transverse ultrasound images. Position of the needle tip in x direction and axial rotation of the needle ϕ are measured using potentiometers placed on needle base outside the tissue. An extended Kalman filter that uses the nonholonomic model and the positional data is implemented to estimate the needle deflection angle θ. In our experiments, we used the 18-gauge flexible notched needles introduced in [10]. Two types of tissue are used in the experiments, plastisol phantom tissue and ex-vivo porcine tissue. The plastisol tissue is made of 80% (by volume) liquid plastic and 20% plastic softener (M-F Manufacturing Co., USA).

Two scenarios are used in the experiments to validate the controller. (1) The needle is steered to reach a target on a straight line placed at a depth of 140 mm. (2) The needle is steered to reach a target at the depth of 140 mm while avoiding a spherical obstacle with a diameter of 2 mm placed at the depth of 70 mm. The 1st scenario is similar to conventional needle insertion in prostate brachytherapy, where the needle should be inserted along a straight line within the tissue. The 2nd scenario represents needle steering when there is a sensitive or impenetrable anatomical obstacle in the proximity of target. In the 2nd scenario we performed a 3 point needle steering. The needle is steered toward a point at $(60, 4, 4)$, next it is steered toward $(80, 4, 4)$ to pass the obstacle, and finally guided to the final destination at $(140, 0, 0)$.

In the experiments, we use condition 1 from Table 1 to steer the needle toward target and later retract the needle on same path and insert again to stabilize the needle on the target point. In the case that requirements of condition 1 is not satisfied conditions 2 and 3 are used. 10 insertions without rotations were performed in each tissue prior to needle steering experiments to identify the nominal curvature of the needle. κ is found by fitting the model in (1) to the experimental results using nonlinear least square method. The magnitude of κ for synthetic and ex-vivo tissue are 0.0023 ± 0.0004 and 0.0015 ± 0.0007 mm^{-1}, respectively. $\pm$ shows 95% confidence bounds. A

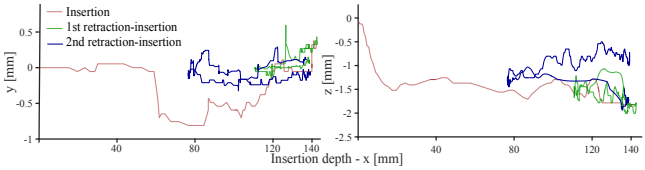
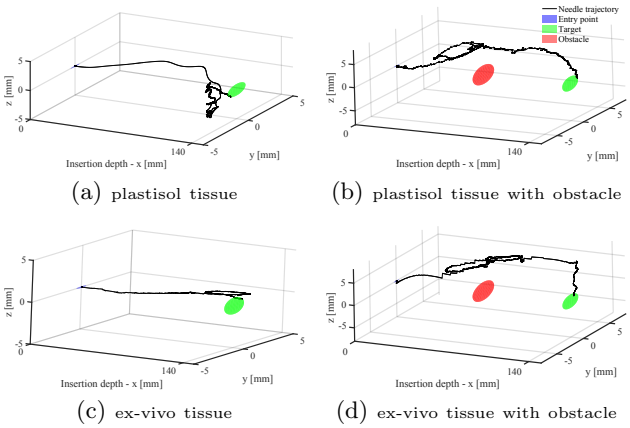


Figure 6. Experimental needle steering result for double retractions on prior insertion paths. Needle deflection in y and z directions are reported.



(a) plastisol tissue (b) plastisol tissue with obstacle

(c) ex-vivo tissue (d) ex-vivo tissue with obstacle

Figure 7. Representative experimental needle steering results for each insertion scenario in synthetic and ex-vivo tissue.

representative result of needle steering using condition 1 is shown in Fig. 6. As it can be seen the controller retracts the needle on previous paths and tries to minimize the error in y direction first and z direction next.

Results of needle steering experiments for each scenario in two tissues are shown in Fig. 7. The magnitude of the targeting error (ϵ in Table 2) is 1 mm and 1.5 mm for needle steering without and with obstacle, respectively. In the representative results shown in Fig. 7, one retraction is performed for needle steering on straight line in both tissues as the error is mainly in y direction. Also, one retraction and two retractions are performed for needle steering with obstacle in plastisol and ex-vivo tissue, respectively.

The experimental results for 10 trials in each tissue are summarized in Table 3. The maximum absolute targeting error in the first and second scenarios are 0.98 and 1.45 mm, respectively, both for insertions in ex-vivo tissue. To furthermore elaborate the effectiveness of the needle steering and for benchmarking the proposed needle insertion strategy, we have performed several fully manual needle insertions in a plastisol tissue and compared the results with the controlled needle insertion. Two skilled brachytherapist were asked to steer the needle to follow a straight line in a synthetic tissue, similar to the one used in previous experiments. The handheld needle steering device used in [10] is used for manual insertions. The surgeon can rotate the needle axially and move the ultrasound probe to locate the needle tip.

Table 3
Results of needle steering experiments for 10 trials.

	Plastisol		Ex-vivo	
	1st Scenario	2nd Scenario	1st Scenario	2nd Scenario
Mean error	0.7	1.13	0.67	1.22
Maximum error	0.91	1.41	0.98	1.45
Standard deviation σ	0.25	0.22	0.31	0.18
Max. of retractions	3	6	4	7
Min. of retractions	0	1	0	2

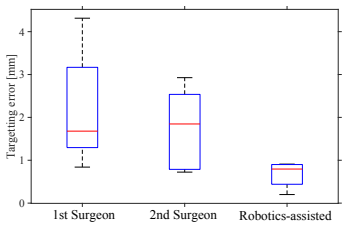


Figure 8. A comparison between robotics-assisted needle steering and manual needle insertion.

Real time visual image feedback of needle tip were provided to the surgeon during the insertions. 10 trials were performed by each surgeon. Results of the manual and controlled needle steering are compared in Fig. 8. The mean targeting error of the controlled needle steering is 60% less than manual needle insertion. Fig. 8 shows that the standard deviation of the error of the proposed approach is smaller than manual needle insertion and the proposed approach shows more repeatability compared to manual needle insertions.

5 Concluding Remarks

In this paper, a 3D needle steering system is developed that can improve needle steering accuracy and extend the application of needle-based interventions to deeper or more difficult-to-reach targets. The controller inserts the needle up to a desired depth in the proximity of the target location, and later performs a retraction and insertion motion that guides the needle toward a desired point. The steering system is capable of compensating for targeting errors in real clinical scenarios by performing multiple retraction/insertions. Accuracy of the needle steering system is 1.41 mm and 1.45 mm for needle insertion in synthetic and ex-vivo tissue.

In the experiments, the obstacle and target are fixed in space rather than fixed to the tissue itself. A small amount of deformation was observed during these experiments, which disturbed the targeting accuracy. Future efforts will focus on validating the controller by performing experiments with biological tissue with moving target since the proposed controller is capable of correcting errors due to tissue motion via retractions. The maximum number of performed retractions directly depend on the uncertainties in the measured value of κ and the desired targeting error. Large uncertainties in the value of κ can increase number of needle retractions, which is

undesirable. In practice, needle curvature can be measured on the fly by means of an online estimator [7,13] or model-based nonlinear observer [5]. One can also relax the constant curvature path assumption by employing a high-level controller that controls the needle curvature through duty-cycling [12,15].

References

[1] Issues in closed-loop needle steering. *Control Engineering Practice*, 62:55 – 69, 2017.

[2] A. M. Bloch. *Nonholonomic Mechanics*, pages 207–276. Springer New York, 2003.

[3] A. M. Bloch, M. Reyhanoglu, and N. H. McClamroch. Control and stabilization of nonholonomic dynamic systems. *IEEE Transactions on Automatic Control*, 37(11):1746–1757, 1992.

[4] R. W. Brockett. Asymptotic stability and feedback stabilization. In *Differential Geometric Control Theory*, pages 181–191. Birkhauser, 1983.

[5] B. Fallahi, C. Rossa, and *et al.* Partial estimation of needle tip orientation in generalized coordinates in ultrasound image-guided needle insertion. In *2016 IEEE International Conference on Advanced Intelligent Mechatronics (AIM)*, pages 1604–1609, 2016.

[6] V. Kallem and N. J. Cowan. Image guidance of flexible tip-steerable needles. *IEEE Transactions on Robotics*, 25(1):191–196, 2009.

[7] M. Khadem, C. Rossa, and *et al.* Semi-automated needle steering in biological tissue using an ultrasound-based deflection predictor. *Annals of Biomedical Engineering*, pages 1–15, 2016.

[8] M. Khadem, C. Rossa, and *et al.* A two-body rigid/flexible model of needle steering dynamics in soft tissue. *IEEE/ASME Transactions on Mechatronics*, 21(5):2352–2364, Oct 2016.

[9] M. Khadem, C. Rossa, and *et al.* Feedback-linearization-based 3d needle steering in a frenet-serret frame using a reduced order bicycle model. In *2017 American Control Conference (ACC)*, pages 1438–1443, 2017.

[10] M. Khadem, C. Rossa, and *et al.* Robotics-assisted needle steering around anatomical obstacles using notched steerable needles. *IEEE Journal of Biomedical and Health Informatics*, pages 1–1, 2017.

[11] Jerrold E. Marsden and Jim Ostrowski. Symmetries in motion: Geometric foundations of motion control. In *Motion, Control, and Geometry: Proceedings of a Symposium*, pages 3–19, 1998.

[12] D.S. Minhas, J.A. Engh, and *et al.* Modeling of needle steering via duty-cycled spinning. In *29th Annual International Conference of the IEEE Engineering in Medicine and Biology Society (EMBS)*, pages 2756–2759, Aug 2007.

[13] Pedro Moreira and Sarthak Misra. Biomechanics-based curvature estimation for ultrasound-guided flexible needle steering in biological tissues. *Annals of Biomedical Engineering*, pages 1–11, 2014.

[14] Wooram Park, Jin Seob Kim, and *et al.* Diffusion-based motion planning for a nonholonomic flexible needle model. In *Robotics and Automation, 2005. ICRA 2005. Proceedings of the 2005 IEEE International Conference on*, pages 4600–4605, 18-22 April 2005.

[15] S. Patil, J. Burgner, and *et al.* Needle steering in 3D via rapid replanning. *IEEE Transactions on Robotics*, 30(4):853–864, Aug 2014.

[16] D.C. Rucker, J. Das, and *et al.* Sliding mode control of steerable needles. *IEEE Transactions on Robotics*, 29(5):1289–1299, Oct 2013.

[17] N.J. van de Berg, D.J. van Gerwen, and *et al.* Design choices in needle steering: A review. *IEEE/ASME Transactions on Mechatronics*, 20(5):2172–2183, Oct. 2015.

[18] M. Waine, C. Rossa, and *et al.* Needle tracking and deflection prediction for robot-assisted needle insertion using 2D ultrasound images. *Journal of Medical Robotics Research*, 01(01):1640001, 2016.

[19] R. Webster, J.S. Kim, and *et al.* Nonholonomic modeling of needle steering. *The International Journal of Robotics Research*, 25(5-6):509–525, 2006.

A Index to Multimedia Extension

The multimedia page is found at
https://youtu.be/ohbtUj96F3Q
The video demonstrates representative results of 3D needle steering experiments.

View publication stats